

RESEARCH ARTICLE

10.1029/2018MS001323

Key Points:

- An isolated cold pool evolving in a dry convective boundary layer is simulated at high resolution
- Sensible heat fluxes are enhanced at the cold pool's edge and suppressed in the center, leading to dissipation from the edge inward
- Land surface interactions reduce the cold pool lifetime, area, and intensity by up to 50% and affect the boundary layer evolution

Correspondence to:

L. D. Grant,
leah.grant@colostate.edu

Citation:

Grant, L. D., & van den Heever, S. C. (2018). Cold pool-land surface interactions in a dry continental environment. *Journal of Advances in Modeling Earth Systems*, 10, 1513–1526. <https://doi.org/10.1029/2018MS001323>

Received 13 MAR 2018

Accepted 29 MAY 2018

Accepted article online 2 JUN 2018

Published online 8 JUL 2018

©2018. The Authors.

This is an open access article under the terms of the Creative Commons Attribution-NonCommercial-NoDerivs License, which permits use and distribution in any medium, provided the original work is properly cited, the use is non-commercial and no modifications or adaptations are made.

Cold Pool-Land Surface Interactions in a Dry Continental Environment

Leah D. Grant¹ and Susan C. van den Heever¹

¹Department of Atmospheric Science, Colorado State University, Fort Collins, CO, USA

Abstract Cold pools influence convective initiation and organization, dust lofting, and boundary layer properties, but little is known about their interactions with the land surface, particularly in dry continental environments. In this study, two-way cold pool-land surface interactions are investigated using high-resolution idealized simulations of an isolated, transient cold pool evolving in a dry convective boundary layer. Results using a fully interactive land surface demonstrate that sensible heat fluxes are suppressed at the center of the cold pool but enhanced at the edge due to the spatial patterns of land surface cooling and the air temperature and wind speed perturbations. This leads to cold pool dissipation from the edge inward. Latent heat fluxes are primarily suppressed within the cold pool, and the magnitude of this suppression is controlled by competition between atmospheric and land surface effects. By comparing the fully interactive land surface simulation to a simulation with imposed surface fluxes, the land surface-cold pool feedbacks are shown to reduce the cold pool lifetime, extent, and intensity by up to 50% and influence the pattern of boundary layer turbulent kinetic energy recovery, which have significant implications for cold pool-induced convective initiation.

1. Introduction

Any time a cloud produces rain, an evaporatively cooled downdraft can form. If this chilled air reaches the surface, it spreads out as a cold pool. This means that cold pools can be found in all of Earth's environments, from moist, tropical oceanic regimes to dry continental regions. Cold pools behave like density currents (Benjamin, 1968; Charba, 1974). They can initiate new convection through lifting at their leading edge and by colliding with other cold pools (Purdom, 1982; Rotunno et al., 1988), interact with boundary layer features (Achtmeier, 1991; Grant & van den Heever, 2016, hereafter GvdH16), and influence convective organization (Gentine et al., 2016; Khairoutdinov & Randall, 2006).

Since cold pools occur at Earth's surface, it is important to consider how the surface interacts with cold pools. In numerical models, cold pool-surface interactions can be represented with varying degrees of complexity. The first and simplest case is of no interactions, in which surface effects on cold pools are completely absent (i.e., no surface energy and momentum fluxes are included). The second simple case is of prescribed surface fluxes. In this scenario, while the surface fluxes do influence the lower atmosphere, the atmosphere does not affect the surface flux magnitudes and spatial patterns, and a land or ocean model is not included. We utilize prescribed fluxes in this study in an experiment called NOFB (NO land-atmosphere FeedBacks). The third, intermediate complexity case is of one-way land-atmosphere interactions. By one-way interactions, we mean that the land or ocean surface properties (e.g., temperature and moisture) are prescribed or held fixed, but the surface flux magnitudes and spatial patterns are influenced by atmospheric variables. The fourth and most complex method is to utilize a fully interactive land surface model in which the surface properties are prognostic, and therefore, both atmospheric and land surface spatiotemporal variability can lead to heterogeneity in surface fluxes. We refer to this scenario as *fully interactive* or *two-way interactive*, and we use this methodology in a simulation called FB (two-way land-atmosphere FeedBacks). Cold pool-land surface interactions in the one- or two-way interactive scenarios may vary considerably depending on the characteristics of the surface, including whether it is water or land, its temperature, and the land's soil and vegetation properties.

Cold pool-ocean surface interactions can be approximated as one-way interactions since the ocean has a large thermal inertia and its surface is always saturated. Indeed, observational (de Szoeke et al., 2017; Johnson & Nicholls, 1983; Saxen & Rutledge, 1998; Young et al., 1995) and modeling studies (Langhans & Romps, 2015; Peters & Hohenegger, 2017; Tompkins, 2001; Trier et al., 1996) have investigated

enhancements in surface sensible heat fluxes (SHFs) and latent heat fluxes (LHFs) in oceanic cold pools. Such enhancements warm and moisten the cold pool with subsequent implications for cold pool dissipation and convective initiation. For example, Trier et al. (1996) simulated a tropical oceanic squall line and concluded that the cold pool-induced surface fluxes notably reduced the cold pool area, ultimately decreasing convective initiation on its fringes later in the squall's lifecycle.

The more complex problem of cold pool-land interactions has received far less attention. Since SHFs can be much larger over land than over ocean, a few studies have investigated the one-way influence of SHFs on cold pools with fixed or prescribed surface properties, including laboratory tank (Linden & Simpson, 1986) and numerical experiments (GvdH16; Robinson et al., 2013). A consensus among these studies is that SHFs slow density current propagation and lead to dissipation. Both Linden and Simpson and GvdH16 attributed this to mixing with turbulent air ahead of the cold pool, which is intensified by surface heating. Peters and Hohenegger (2017) also investigated one-way influences of surface fluxes on squall line cold pools, but for a saturated surface. They did not find any significant impacts of the surface fluxes on the cold pools because the continual replenishment of evaporatively cooled air overwhelmed any surface flux effects.

Only a handful of studies have discussed cold pool properties in simulations with two-way land-atmosphere interactions (Del Genio et al., 2012; Drager & van den Heever, 2017, hereafter DvdH17; Gentine et al., 2016; Schlemmer & Hohenegger, 2016). Del Genio et al. showed using bulk statistics that, contrary to oceanic cases, surface fluxes were suppressed within tropical continental cold pools because the land surface under the cold pools rapidly cooled. DvdH17 investigated spatiotemporal variability in tropical continental cold pools; they demonstrated suppressed (enhanced) SHFs (LHFs) in the cold pool center because the ground was cooled and soaked by the rainy downdraft that generated the cold pool. Both of these studies were of moist tropical environments, and the other two studies (Gentine et al., 2016; Schlemmer & Hohenegger, 2016) did not discuss the land responses. Additionally, all of these studies were conducted using horizontal grid spacings of 500 m to 1 km. However, GvdH16 showed that surface flux impacts on cold pools can be different at large-eddy simulation (LES) grid spacings of 50–100 m or less.

Evidently, a major knowledge gap exists regarding two-way cold pool-land interactions, especially in semiarid environments—a particularly interesting scenario because of the low thermal inertia of drier land. Moreover, these interactions have not been investigated at fine spatial and temporal resolutions. Therefore, the goal of our study is to address the following two questions: (1) how does a cold pool influence the land surface in dry continental environments, in the absence of cloud effects such as precipitation and anvil shading, and (2) how do interactions between the cold pool and the land surface alter the subsequent evolution of the cold pool and the boundary layer in which it is developing? We address these questions with idealized 3-D LES simulations of cold pools over a dry continental surface. An isolated cold pool is introduced into a convective boundary layer (CBL) developing over a fully interactive land surface, and the subsequent evolution of the land surface properties is analyzed to answer the first question. To address the second question, two simulations are compared, one with the fully interactive land surface and one with prescribed, horizontally homogeneous surface fluxes. We show by comparing these two simulations that the cold pool-land surface interactions play a substantial role in the evolution of both the cold pool and the CBL, with implications for the representation and simulation both of cold pools and land surface processes in numerical models.

2. Model Setup and Initialization

We first examine the land surface's response to the cold pool in an LES simulation with a fully interactive land surface. The simulation was conducted with the Regional Atmospheric Modeling System version 6.1.18 (Cotton et al., 2003; Saleeby & van den Heever, 2013), which is coupled to the Land Ecosystem-Atmosphere Feedback (LEAF) land surface model, version 3 (Walko et al., 2000). LEAF prognoses soil and vegetation temperature and water content, including the effects of surface-atmosphere exchange (following the parameterization by Louis, 1979; Louis et al., 1981), radiative fluxes, and precipitation, although precipitation is not considered here.

We use 50-m horizontal grid spacing, a constant 20-m vertical grid spacing throughout the lowest 4 km and a stretched grid above this altitude to a maximum of 100-m vertical grid spacing, and a 0.5-s time step for the LES simulation. Such grid spacings permit adequate representation of the cold pool's turbulent

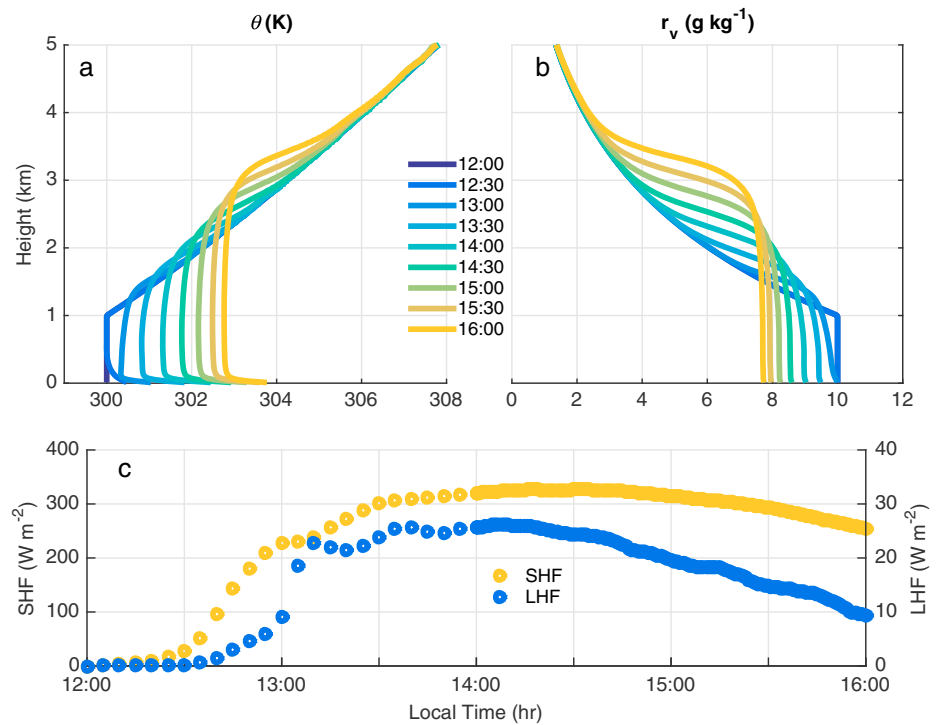


Figure 1. Environmental profiles of (a) θ and (b) r_v every 30 min from 12:00 to 16:00 LT for simulation FB. Environmental quantities are defined as averages between 40 and 80 km away from the domain center. (c) Time series of environmental sensible heat flux (SHF) and latent heat flux (LHF) in the FB simulation. FB = two-way land-atmosphere FeedBacks.

characteristics and interactions with the surface (Bryan et al., 2003; GvdH16). The 3-D channel domain size of $200 \text{ km} \times 20 \text{ km} \times 10 \text{ km}$ is composed of $4001 \times 401 \times 294$ points. Water vapor is not allowed to condense; that is, microphysical processes are not activated, which eliminates the influence of cloud feedbacks on the analysis of cold pool-land surface interactions, thus allowing us to focus specifically on the two questions we aim to answer.

In LEAF, a semidesert vegetation class with a vegetation fraction of 0.2 and a normalized difference vegetation index of 0.1 are used to represent an idealized semiarid climate like northern Africa, the southwestern United States, or Australia. Eight soil levels from 5 cm to 1.2 m in depth are utilized. The soil temperature is initialized to be 10 K warmer than the lowest atmospheric level at the shallowest layer, and the soil temperature offset decreases exponentially with increasing depth at a scale depth of 15 cm. The soil moisture is initialized to 20% saturation fraction at all depths. Soil-atmosphere energy exchanges are communicated through the canopy layer. The canopy layer is the vegetation or, for nonvegetated areas, the air properties at the roughness height. Other physical parameterizations include the Harrington (1997) radiation scheme updated every five simulations minutes and a Smagorinsky (1963) turbulence scheme with stability modifications by Lilly (1962) and Hill (1974). A Rayleigh damping layer is included above 7 km above ground level (AGL).

Before the cold pool is introduced, the simulation is integrated for 2 hr, from 12:00 to 14:00 local time (LT), thereby allowing the CBL to fully develop. The initial conditions at 12:00 LT include a constant water vapor mixing ratio (r_v) of 10 g/kg and a constant potential temperature (θ) of 300 K over the lowest 1 km, and a surface pressure of 1000 hPa. Weakly stable conditions above 1 km are characterized by a constant Brunt-Väisälä frequency N_v , defined by $N_v^2 = \frac{g}{\theta_v} \frac{d\theta_v}{dz} = 5 \times 10^{-5} \text{ s}^{-2}$ where θ_v is the virtual potential temperature (e.g., Emanuel, 1994), and an exponentially decreasing r_v profile with a scale height of 2 km. The initial θ and r_v profiles at 12:00 LT are shown in Figures 1a and 1b. The initial wind profile is calm. For radiation calculation purposes, the date and latitude used in this simulation are 1 April and 20°N. Random θ perturbations are introduced over the lowest 500 m with a magnitude of 0.25 K that decreases linearly with height in order to break the horizontal homogeneity. Periodic lateral boundary conditions are used in both the zonal and

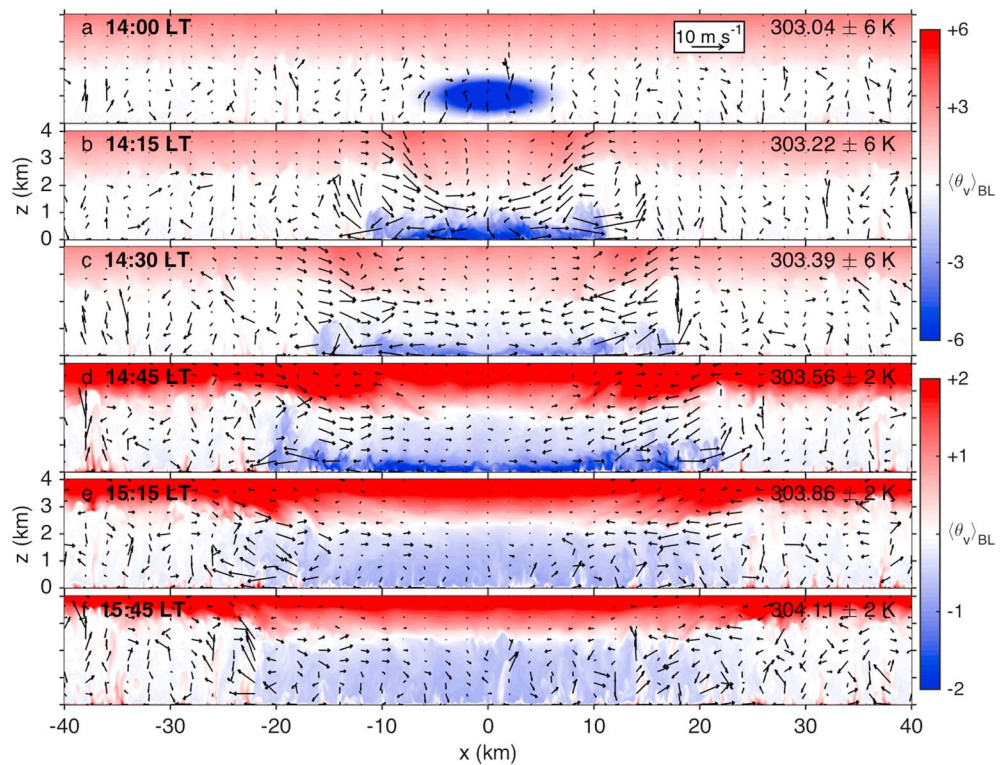


Figure 2. Instantaneous cross sections of θ_v (shaded) and $[u, w]$ wind vectors through the domain center at different times for simulation FB. The color bar in each panel is centered on $\langle \theta_v \rangle_{BL}$ (the 0–2 km above ground level and environmental average of θ_v), which is listed in the upper right of each panel along with the color bar limits. The wind vector legend is provided in panel (a). Note the change in the color bar limits from panels (a)–(c) to panels (d)–(f), and the change in time interval of 15 min for (a)–(c) to 30 min for (d)–(f).

meridional directions. Model output is saved every five simulation minutes during this 2-hr time period. Over the course of the 2 hr, the CBL deepens to ~ 2 km (Figures 1a and 1b). By 13:30 LT, SHFs and LHF are increased to average values of 300 and 25 W/m^2 , respectively (Figure 1c). The CBL profiles and surface flux magnitudes are representative of observations in semiarid climates (e.g., Couvreux et al., 2012). The CBL gradually warms both from the SHFs and from entrainment of warmer free-tropospheric air, but it also dries because the entrainment of the drier free-tropospheric air outweighs the moistening by LHF from the surface.

At 14:00 LT, a cold pool is introduced by adding a cold, dry, line-oriented bubble that is independent of the y direction and therefore extends across the entire y dimension. Hereafter, this simulation will be referred to as the FB simulation (two-way land-atmosphere FeedBacks included). The cold bubble is described by a cosine function with a vertical radius of 1 km, a horizontal (x direction) radius of 8 km, and a perturbation $\theta(r_v)$ amplitude of -10 K (-10%) that is centered at 1 km AGL and at the domain center (Figure 2a). The cold bubble's line-type structure is representative of a cold pool created by linearly oriented convection or a large cold pool for which curvature along its edge can be neglected. The dry perturbation represents the transport of drier air from above the CBL by a downdraft. The zonal boundary conditions are changed to open-radiative (Klemp & Wilhelmson, 1978) so that gravity waves excited by the cold pool can exit through the east and west boundaries, but the meridional boundary conditions are kept periodic. The linear cold bubble falls to the surface and spreads out in the x direction over the course of 2 hr, during which model output is saved every minute. The simulations were performed on the Yellowstone supercomputing system (Computational and Information Systems Library, 2012).

A number of different cold pool initialization methods were tested in addition to the setup described above including a circular versus linear cold pool, different land surface types and initial soil moisture values, and

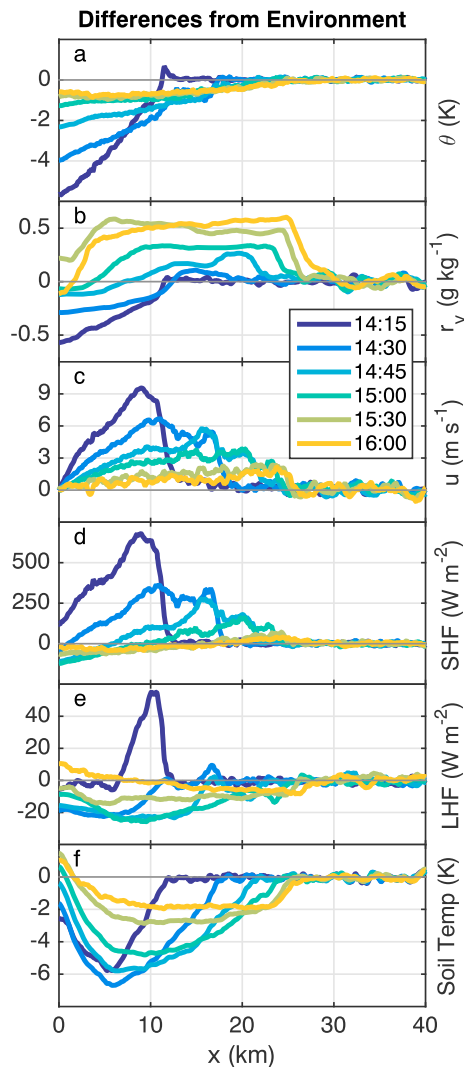


Figure 3. Composite line plots of perturbations relative to the environment every 15 min from 14:15 to 15:00 LT and every 30 min from 15:00 to 16:00 LT (see legend). Panels (a)–(c) show quantities at the lowest atmospheric level (10 m above ground level), and panels (d)–(f) show land surface quantities (soil temperature is for the shallowest soil layer). Composites were created by averaging in the y direction and then averaging the right half of the domain with a mirror image of the left-half of the domain. Hence, u in panel (c) is the wind component away from the domain center. SHF = sensible heat flux; LHF = latent heat flux.

is the opposite response to that shown in Del Genio et al. (2012) for a moist tropical continental environment. The peak magnitude of this enhancement varies substantially with the cold pool's age. SHFs remain enhanced by 20 to 75 W/m^2 between $x = 20$ and 25 km even at 15:30 and 16:00 LT, after the cold pool's structure is no longer distinguishable and it has stopped propagating (Figure 2). While the simulated SHF enhancements near the cold pool edge cannot be validated against observations of fluxes in continental cold pools given the lack of such data, several recent studies presenting observational estimates of SHFs from thermal imagery demonstrate rich spatial variability even in the absence of cold pool effects (Lee et al., 2017; Morrison et al., 2017). Figure 7 in Morrison et al. (2017) shows sensible heat flux variations of several hundred W/m^2 over distances of 10 m or less, suggesting that the magnitude of the SHF enhancements within our simulated cold pools is reasonable. The SHF enhancement near the cold pool edge is strongly correlated with the near-surface wind speed (compare panels c and d in Figure 3), but its magnitude is

varying initial bubble shapes and configurations, among others. The results and trends described in sections 3 and 4 were found to be robust for the different initial configurations. We also emphasize that, since microphysical processes are excluded, the cold pool and environment in these experiments best represents a dissipating, transient cold pool, and not a cold pool that is actively and continuously replenished by evaporative cooling in association with a long-lived convective system like a squall line. Finally, the cold pool was introduced at 14:00 LT as this represents a reasonable time of day during which cold pools form, although larger cold pools might be more common at later afternoon or evening times. Since surface fluxes tend to peak after 12:00 LT, the cold pool-land surface interactions discussed in the following sections may represent an upper limit on their magnitudes.

3. Land Surface Response to the Cold Pool

Key aspects of the FB simulation are illustrated by the instantaneous cross sections shown in Figure 2. The typical head structure and its associated circulation are obvious for the first 45 min (Figures 2b–2d). After 45 min, the cold pool's structure is no longer well defined, though the remnant circulation remains evident throughout the simulation. A persistent circulation but lack of well-defined temperature structure was also seen in sea breeze simulations subject to gradual heating in Robinson et al. (2013). Turbulent features of the cold pool (such as Kelvin-Helmholtz waves) and of the CBL (such as convective plumes originating from the surface) are evident throughout the 2 hr. Mixing by these features leads to dissipation of the cold pool (GvdH16). The cold pool reaches 25 km from the domain center after 1 hr (15:00 LT), at which point it no longer propagates outward (compare panels e and f in Figure 2). The coldest perturbations are found nearer the center of the cold pool. Finally, we see that the cold pool's influence on the mean CBL temperature and depth persists even after the cold pool has dissipated (Figures 2e and 2f).

Both the land surface and the near-surface atmospheric properties show signatures of the cold pool's presence that vary through time, as indicated in Figure 3. All quantities shown are perturbations relative to the environment, where the environmental quantities are defined as averages between 40 and 80 km away from the domain center in both the positive and negative x direction. This environmental definition avoids both the center of the domain that is influenced by the cold pool and the 20 km near the lateral boundaries. We focus first on the SHF response to the cold pool. SHFs are always enhanced relative to the environment near the leading edge of the cold pool (Figure 3d), which

modulated by the surface-air temperature difference as dictated by the near-surface air temperature (Figure 3a) and the soil temperature (Figure 3f).

SHFs are not always enhanced within the cold pool, however. After 45 min to 1 hr (14:45–15:00 LT), SHFs at the domain center are suppressed relative to the environment by up to 120 W/m^2 . The suppressed SHF region extends to $x = 9.5 \text{ km}$ after 1 hr and to $x = 17.5 \text{ km}$ after 2 hr (16:00 LT) when its magnitude has decreased to around 50 W/m^2 (Figure 3d). Notice that soil temperatures are most strongly suppressed from $x = 2\text{--}15 \text{ km}$ over the first hour, where the accumulated SHFs are greatest (compare panels d and f in Figure 3), and that the cool soil temperature anomaly persists for longer than the cool air temperature anomaly (compare panels a and f in Figure 3). The temporal lag in the soil temperature's response to the cold pool, in combination with slower wind speeds near the center as the peak winds expand outward in time, explain the persistent suppressed SHFs nearer the center of the aged cold pool.

To investigate the SHF perturbation patterns more quantitatively, a perturbation analysis was performed. In LEAF, the SHF is calculated following Louis (1979) and Louis et al. (1981) as

$$\text{SHF} = \rho_0 c_p a^2 f_h U (\theta_c - \theta_a) \quad (1)$$

where ρ_0 is the base state air density at the surface, c_p is the air heat capacity at constant pressure, a^2 is the drag coefficient in neutral conditions (here a constant because the roughness length is a constant), f_h is the stability function modification to the drag coefficient that depends on the near-surface stability and wind speed via the Richardson number, U is the magnitude of the wind speed at the lowest model level (here, 10 m AGL), θ_c is the canopy potential temperature (canopy temperature is the temperature of the vegetation or, in the case of bare soil, the air temperature at the roughness height; recall that soil-atmosphere exchanges are communicated through the canopy layer), and θ_a is the air potential temperature at the lowest model level.

Sensible heat flux perturbations in the cold pool were analyzed by decomposing each variable in equation (1) into an environmental mean component (denoted with the subscript 0 for the purposes of this analysis) and a perturbation component (denoted with a prime), similar to prior work investigating oceanic fluxes (e.g., Chuda et al., 2008; Saxen & Rutledge, 1998) except that here, θ_c represents an additional variable and θ_c' only appears in the perturbation analysis for simulations including two-way land-atmosphere interactions:

$$\text{SHF} = \rho_0 c_p a^2 (f_{h0} + f_h') (U_0 + U') [(\theta_{c0} + \theta_c') - (\theta_{a0} + \theta_a')] \quad (2)$$

Equation (2) is rearranged as follows:

$$\text{SHF} - \langle \text{SHF} \rangle = \rho_0 c_p a^2 \left[\begin{array}{l} \underbrace{f_{h0} U_0 (\theta_{c0} - \theta_{a0})}_{\text{SHF}_0 \text{ term}} - \langle \text{SHF} \rangle + \underbrace{f_{h0} U' (\theta_{c0} - \theta_{a0})}_{U' \text{ term}} \\ + \underbrace{f_h' U_0 (\theta_{c0} - \theta_{a0})}_{f_h' \text{ term}} + \underbrace{f_{h0} U_0 \theta_c'}_{\theta_c' \text{ term}} + \underbrace{-f_{h0} U_0 \theta_a'}_{\theta_a' \text{ term}} \\ + \underbrace{f_h' U' (\theta_{c0} - \theta_{a0})}_{U' f_h' \text{ term}} + \underbrace{f_{h0} U' \theta_c'}_{U' \theta_c' \text{ term}} + \underbrace{-f_{h0} U' \theta_a'}_{U' \theta_a' \text{ term}} \\ + \underbrace{f_h' U_0 \theta_c'}_{\theta_c' f_h' \text{ term}} + \underbrace{-f_h' U_0 \theta_a'}_{\theta_a' f_h' \text{ term}} + \underbrace{f_h' U' (\theta_c' - \theta_a')}_{O(3)' \text{ terms}} \end{array} \right] \quad (3)$$

where $\langle \text{SHF} \rangle$, the total SHF averaged over the environmental region, has been subtracted from both sides such that the left-hand side of equation (3) represents the SHF perturbation within the cold pool. The right-hand-side terms represent contributions to total SHF perturbations by individual perturbations, covariances between two variables, and third-order covariance terms. Note that, interestingly, $\langle \text{SHF} \rangle \neq \text{SHF}_0$ due to nonlinear covariances between U' and f_h' (see Figures 4a and 4c), necessitating the two different notations for $\langle \text{SHF} \rangle$ and SHF_0 .

Each term in equation (3) is shown in Figures 4a and 4c as a composite at two different times, one early (panel a) and one later on (panel c) in the cold pool's lifetime. Each term is normalized by the maximum SHF perturbation value so as to evaluate their relative contributions to the cold pool SHF perturbations.

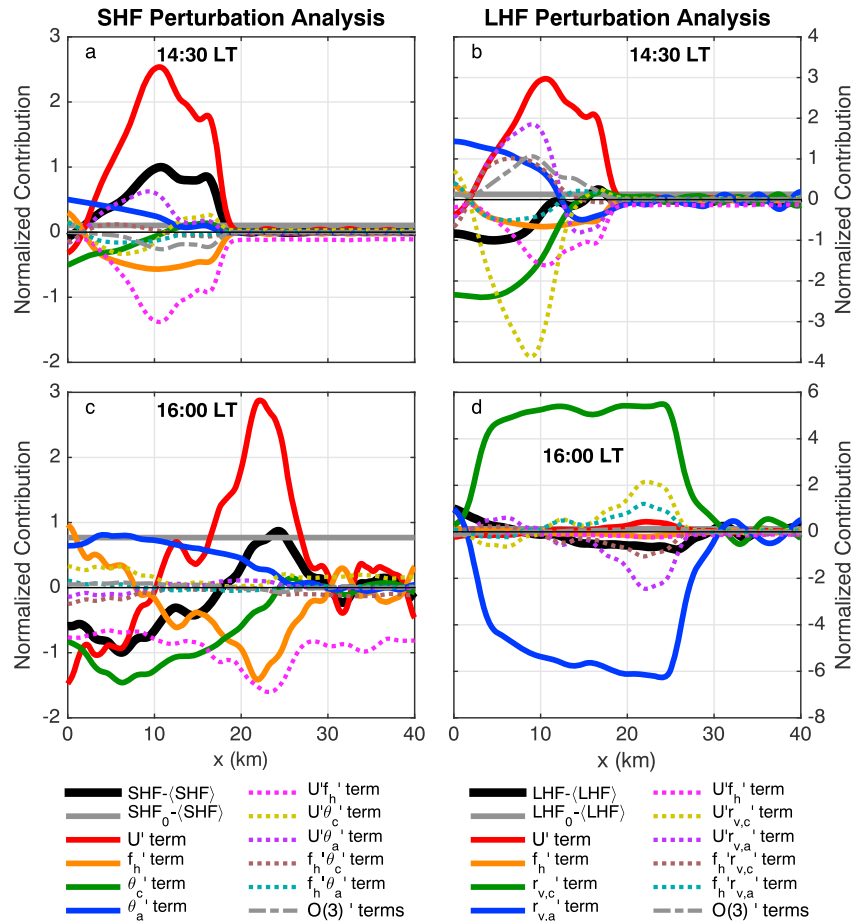


Figure 4. Composite line plots of terms contributing to (a, c) SHF perturbations from equation (3) as indicated in the left legend and (b, d) LHF perturbations from equation (4) as indicated in the right legend. Perturbations are shown at (a, b) 14:30 LT and (c, d) 16:00 LT. All composites were smoothed using a 1-2-1 filter with a span of 3 km and then normalized by the maximum value of $[SHF - \langle SHF \rangle]$ or $[LHF - \langle LHF \rangle]$. SHF = sensible heat flux; LHF = latent heat flux.

Near the leading edge of the cold pool, the primary contributor to the positive SHF perturbation is the wind speed enhancement (red solid line). However, the magnitude of the U' term is 2 to 3 times larger than the actual SHF perturbation shown by the solid black line. Therefore, the negative terms near the cold pool edge are important for modulating the wind speed-induced enhancement in sensible heat fluxes, including the f_h' and the $U'f_h'$ terms (orange solid and pink dashed lines, respectively). Other terms that are also important for the positive SHF perturbations include air temperature perturbations and their covariations with wind perturbations, especially when the cold pool is younger (Figure 4a). In summary, during the early stages of the cold pool and near its leading edge, the atmospheric variable perturbations are the most important contributors to the enhanced SHFs. This qualitative effect would be captured by one-way land-atmosphere interactions and was in fact demonstrated in GvdH16 and Gentine et al. (2016).

Toward the center of the cold pool, Figures 4a and 4c demonstrate that the canopy temperature perturbation (green solid line) is the most important contributor to the suppressed SHFs at all stages of the cold pool lifetime, although canopy temperature perturbations are especially important later on (Figure 4c). The negative θ_c' is largely responsible for widening the area of negative SHF perturbations at the cold pool center compared to what would be expected from the individual effects of wind speed and air temperature perturbations. Such an effect cannot be captured with one-way land-atmosphere interactions in which θ_c is fixed or prescribed. Overall, this analysis demonstrates that the fully interactive land surface is very important in determining the spatiotemporal patterns and magnitudes of the SHF perturbations under the cold pool.

This importance is manifest through the variable soil and canopy temperatures, as well as through impacts on the exchange coefficient through the stability function.

LHFs are generally suppressed within the cold pool relative to the environment, except near the cold pool's leading edge for the first 30 min (Figure 3e). We can quantitatively examine the contributions to the LHF perturbations in the same manner as the SHF perturbations. The LHF perturbation equation ((4), below) is exactly analogous to the SHF perturbation equation (3), except with c_p replaced with L_v (the latent heat of vaporization), θ_c replaced with $r_{v,c}$ (the canopy water vapor mixing ratio), and θ_a replaced with $r_{v,a}$ (the air water vapor mixing ratio at the lowest model level):

$$\text{LHF} - \langle \text{LHF} \rangle = \rho_0 L_v a^2 \left[\begin{array}{l} \underbrace{f_{h0} U_0 (r_{v,c0} - r_{v,a0})}_{\text{LHF}_0 \text{ term}} - \langle \text{LHF} \rangle + \underbrace{f_{h0} U' (r_{v,c0} - r_{v,a0})}_{U' \text{ term}} \\ + \underbrace{f_h' U_0 (r_{v,c0} - r_{v,a0})}_{f_h' \text{ term}} + \underbrace{f_{h0} U_0 r_{v,c}'}_{r_{v,c}' \text{ term}} + \underbrace{-f_{h0} U_0 r_{v,a}'}_{r_{v,a}' \text{ term}} \\ + \underbrace{f_h' U' (r_{v,c0} - r_{v,a0})}_{U' f_h' \text{ term}} + \underbrace{f_{h0} U' r_{v,c}'}_{U' r_{v,c}' \text{ term}} + \underbrace{-f_{h0} U' r_{v,a}'}_{U' r_{v,a}' \text{ term}} \\ + \underbrace{f_h' U_0 r_{v,c}'}_{r_{v,c}' f_h' \text{ term}} + \underbrace{-f_h' U_0 r_{v,a}'}_{r_{v,a}' f_h' \text{ term}} + \underbrace{f_h' U' (r_{v,c}' - r_{v,a}')}_{O(3)' \text{ terms}} \end{array} \right] \quad (4)$$

Each term in equation (4) is shown in Figures 4b and 4d at the same early and later times as the corresponding SHF perturbation analysis, and the terms are again normalized in order to evaluate their relative contributions to the total LHF perturbation. Figure 4b demonstrates that the early LHF peaks at the cold pool's leading edge are a result of the wind speed perturbations (red solid line; also compare panels c and e in Figure 3). Nearer the center of the cold pool where the LHFs are suppressed, the most important terms are the air and canopy mixing ratio perturbations (blue and green solid lines, respectively) and their respective covariations with wind perturbations (purple and gold dashed lines). The $r'_{v,a}$ term contributes positively to LHF perturbations because the cold pool is initially drier than the environment, thereby helping to enhance the surface-air moisture gradients. However, the $r'_{v,c}$ term contributes negatively to LHF perturbations because the early LHF peaks have removed water from the soil under the cold pool, thereby leading to reduced canopy mixing ratios and weaker surface-air moisture gradients. The $r'_{v,c}$ terms are larger in magnitude than the $r'_{v,a}$ terms, leading to an overall LHF suppression.

As the cold pool ages, LHFs are almost always suppressed within the cold pool relative to the environment (Figure 3e). The LHF perturbation analysis at 120 min (Figure 4d) indicates that the air and canopy mixing ratio perturbations are by far the most important contributors. The $r'_{v,c}$ term contributes positively to LHF perturbations because over the course of the 2 hr, the primarily suppressed LHFs have resulted in less net evaporation from the soil under the cold pool than in the environment, and hence higher soil moisture under the cold pool (note that this is the opposite response to that at 30 min shown in Figure 4b). However, the $r'_{v,a}$ term is negative because the cold pool air is more moist than the environmental air (Figure 3b), which acts to weaken the surface-air moisture gradients. The enhanced water vapor in the cold pool can be explained by the differential CBL growth (Figure 2). Within the stable cold pool, CBL growth is suppressed and water vapor remains steady. On the other hand, in the environment, the CBL dries as its depth increases (Figure 1b) because the entrainment of drier free-tropospheric air outweighs moistening by LHFs. This leads to a positive water vapor perturbation in the cold pool that grows in time. The $r'_{v,a}$ term is larger in magnitude than the $r'_{v,c}$ term, resulting in suppressed LHFs. Overall, Figures 4b and 4d suggest that the two-way interactive land surface is important in modulating the magnitude of the cold pool LHF perturbations.

To summarize, we have addressed the first question in this section by investigating the land surface's response to the cold pool. In particular, we documented the spatial and temporal variability in SHF and LHF patterns and land surface properties, as well as explored the mechanisms explaining these variations through SHF and LHF perturbation analysis and physical reasoning. The perturbation analysis demonstrated the importance of the fully interactive land surface (θ'_c and $r'_{v,c}$ terms) in influencing the spatiotemporal surface flux patterns.

4. Cold Pool-Land Surface Feedbacks

While we have shown that the cold pool does influence the surface fluxes (particularly the SHFs) and that land surface perturbation terms are important contributors to the spatial and temporal SHF and LHF patterns, it is unclear to what extent the feedbacks between the atmosphere and the fully interactive surface affect the cold pool's subsequent evolution. For instance, the enhanced SHFs near the edge and suppressed SHFs near the center should result in cold pool dissipation from the edge inward; however, the cold pool could dissipate from the edge inward regardless of the SHF pattern, simply through turbulent mixing between the cold pool air and the CBL plumes which is most vigorous at the edge. This brings us to our second question: How do interactions between the cold pool and the land surface subsequently influence the evolution of both the cold pool and the CBL? To address this question, an additional simulation called NOFB (NO land-atmosphere FeedBacks) is performed. NOFB is identical to FB in all respects except that the cold pool-surface flux interactions are removed by imposing spatially uniform but time-varying SHFs and LHFs. The imposed surface flux values are the environmental averages from the FB simulation (Figure 1c) such that the energy input to the boundary layer is held constant between the FB and NOFB simulations. As a result, the CBL statistics in the environment ahead of the cold pool are nearly identical between the FB and NOFB runs (not shown), a critical consideration because of the important role that turbulent mixing plays in cold pool evolution (Linden & Simpson, 1986; GvdH16). Therefore, the differences between the FB and NOFB simulations are entirely attributable to the cold pool-land surface interactions. Similar sensitivity test methodologies have also been utilized in prior studies (Rieck et al., 2014; GvdH16; Gentine et al., 2016).

Figure 5, which details a comparison between the FB and NOFB simulations, reveals that the two-way cold pool-land surface interactions do exert a significant influence on the cold pool's evolution. One of the most obvious differences between the two simulations is in how far the cold pool propagates. Recall that in FB, the cold pool stops propagating after an hour, when it has reached ~25 km from the center. However, in NOFB, the cold pool propagates faster and continues to propagate outward throughout most of the 2 hr (Figure 5b). The cold pool dissipation timescale is therefore about twice as long in the NOFB simulation compared to the FB simulation. The propagation differences translate to a 60% increase in final cold pool extent in NOFB (Figure 5d).

Cold pool propagation speed is related to cold pool intensity, or integrated negative buoyancy, which we calculate from the composite fields as $C^2 = 2 \int_0^D -B dz$ (Benjamin, 1968), where C is the intensity, $B = g \frac{\theta'_v}{\langle \theta_v \rangle}$ is the buoyancy, $\langle \theta_v \rangle$ is the environmental average profile of θ_v , and the cold pool top D is defined as the lowest altitude where $u = 0$ (the lingering effects of the cold pool on B after it has dissipated preclude us from using a buoyancy threshold to define D). C is calculated only for columns where $D < 2$ km and where $B < -0.005 \text{ m}^2/\text{s}^2$ somewhere below D , otherwise, C is set to 0. Figure 5d indicates that the maximum intensity increases in NOFB by up to 30%, in keeping with its faster propagation. A similar story is evident in the near-surface temperatures: minimum θ_v perturbations are 10–30% stronger throughout the first hour, and the entire cold pool is colder for the first 35 min in NOFB compared to FB (Figure 5c). In the FB simulation, the cold pool's faster dissipation, smaller extent, and weaker intensity are all attributable to the enhanced SHFs near its leading edge, which warm the cold pool air and hasten its dissipation. It is worth noting that such effects could also be found using prescribed surface properties and hence only one-way land-atmosphere interactions, because the enhanced SHFs near the cold pool's leading edge are primarily due to increased wind speed (Figure 4). The enhanced dissipation was demonstrated in GvdH16 and Gentine et al. (2016). Interestingly, the influence of enhanced SHFs within the cold pool is much larger here than in GvdH16, perhaps because the cold pools did not propagate into an active boundary layer in that study.

Recall that in FB, SHFs are always enhanced near the edge but are eventually suppressed in the center of the remnant cold pool. Such a pattern should lead to dissipation of the cold pool from the edge inward, and indeed, this is the case, as can be inferred by the slope of the θ'_v contours (Figure 5a). On the other hand, in NOFB, the θ'_v contours slope in the opposite direction between $x = 0$ –20 km (Figure 5b), meaning that the cold pool dissipates from the center outwards. As a result, despite the colder temperatures throughout most of NOFB compared with FB, temperatures are actually warmer in the center of the NOFB cold pool starting at 35 min into the cold pool lifecycle (Figure 5c).

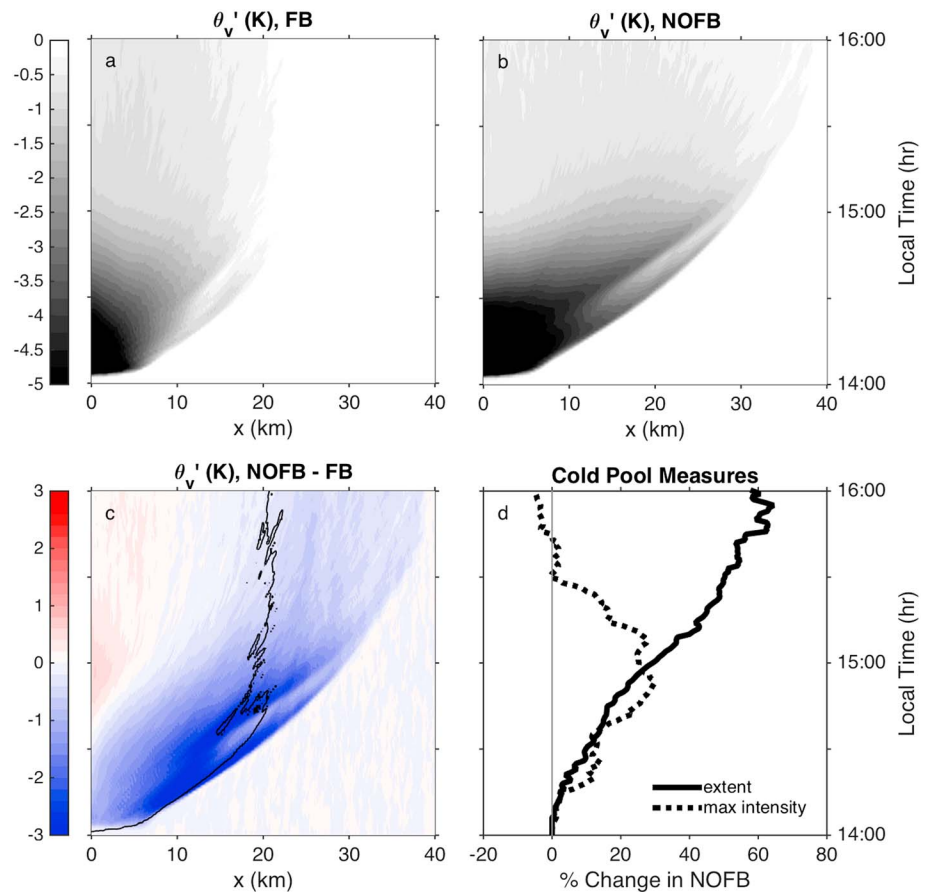


Figure 5. Composite Hovmöller of θ_v' relative to the environment at 10 m above ground level for (a) FB, (b) NOFB, and (c) NOFB minus FB. In (c), the -0.25 K θ_v' contour for FB is included for comparison. (d) Percent increase in composite cold pool extent, and in maximum composite intensity (C) within 10 km of the leading edge, as a function of time in simulation NOFB relative to FB. Cold pool extent is defined as the farthest distance from the domain center where $C > 0$. See text for the definition of C . FB = two-way land-atmosphere FeedBacks; NOFB = NO land-atmosphere FeedBacks.

The difference in evolution between the FB and NOFB cold pools that arises due to the inclusion of a fully interactive surface ultimately affects the CBL structure (Figure 6). We show the 15:00–15:30 LT period because the CBL is beginning to recover and differences in CBL structure between the two cases are most clear. The recovery of turbulent kinetic energy (TKE) and CBL depth to their ambient conditions is slowest near the center of the FB cold pool, since TKE decreases in intensity toward the cold pool center (Figure 6a). The slowest recovery in the center coincides with the region of suppressed SHFs throughout the second hour (Figure 3d). Note that this spatial TKE pattern would *not* be properly captured using only one-way land-atmosphere interactions because the canopy temperature perturbation plays a critical role in the suppressed SHFs at the cold pool center (Figure 4). But in NOFB, the TKE and CBL depth are most suppressed from $x = 10$ – 25 km, while TKE increases in intensity from $x = 15$ km toward the center (Figure 6b). The faster TKE recovery in the NOFB cold pool's center coincides with the warmer θ_v' values compared to the FB case (Figure 5c) and results both from the lack of spatial variability in SHFs and from the advection of cooler temperatures away from the center by the cold pool circulation.

Another clear difference between the two CBLs is the magnitude of peak TKE intensity. In both cases, a local TKE maximum appears within and near the leading edge of the cold pool in association with shear in the mean circulation (Figure 6). However, the magnitude of the TKE maximum is noticeably greater in FB than in NOFB. Some of the apparent increase in magnitude results from a slight smearing of the NOFB composite TKE because the NOFB cold pool is still propagating outward during this time period. However, the peak composite TKE intensity at individual times is more intense (by up to 35%) in the FB case than in the NOFB case

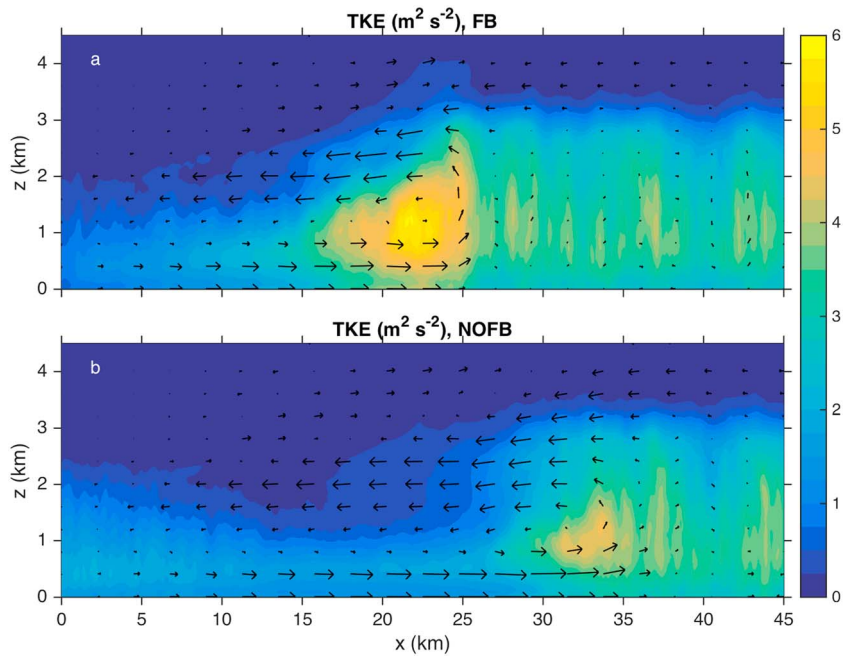


Figure 6. Cross sections of composite TKE (shaded) and $[u,w]$ wind vectors, averaged over 15:00–15:30 LT, for (a) FB and (b) NOFB. $\text{TKE} = 0.5(u'^2 + v'^2 + w'^2)$ and perturbation wind components are calculated at each time by subtracting the y average. TKE = turbulent kinetic energy; FB = two-way land-atmosphere FeedBacks; NOFB = NO land-atmosphere FeedBacks.

throughout the second hour. The enhanced SHFs near the leading edge of the remnant cold pool in FB lead to greater near-surface available energy, locally more vigorous and turbulent convective plumes, and the resultant greater TKE intensity seen in Figure 6. The boundary layer is also locally deeper there. This means that the cold pool could initiate new convection even after its buoyancy anomaly has dissipated, an effect that is enhanced with an interactive surface.

5. Summary and Implications

This study, to our knowledge, represents the first investigation of the land surface's response to cold pools in dry environments and is the first to explicitly demonstrate the significant impacts of a fully interactive land surface on the *process-scale* evolution of both the cold pool and the boundary layer in such an environment. Specifically, we aimed to answer two questions: (1) How does a cold pool influence the land surface in a dry continental environment in the absence of cloud influences like rain and anvil shading? And (2) how do interactions between the cold pool and land surface subsequently influence the evolution of the cold pool and the CBL? To investigate these questions, we performed idealized LES simulations of isolated, dissipating cold pools in a daytime, dry-continental CBL, in which microphysical processes were excluded. Two simulations were examined, one with a fully interactive land surface and one with imposed surface fluxes. In the interactive surface simulation, we found that SHFs were always enhanced near the cold pool edge, largely due to stronger wind speeds—an effect that can therefore also be represented using fixed surface properties, that is, using one-way land-atmosphere interactions. However, SHFs were suppressed near the cold pool's center later in its lifetime due to cooler land surface temperatures, a result that can only be properly represented with two-way land-atmosphere interactions. LHF were generally suppressed within the cold pool because r_v was higher in the cold pool than in the environment. The positive r_v perturbations resulted from suppressed CBL growth and therefore reduced boundary layer entrainment drying in the cold pool region. The effect of greater cold pool moisture on the LHF perturbations was, however, countered by higher soil moisture under the cold pool, which in turn resulted from the suppressed LHF. Therefore, the fully interactive land surface modulated the magnitude of the LHF perturbations in the cold pool.

We found by comparing the interactive land surface case to the prescribed fluxes simulation that the cold pool-land surface feedbacks exert a strong influence on the cold pool evolution. When a fully interactive land surface was used, the cold pool was weaker throughout its lifetime and therefore propagated more slowly, dissipated twice as quickly, and was nearly 40% smaller in extent compared to the prescribed fluxes case. These significant changes were attributed to the enhanced SHFs near the cold pool's leading edge in the interactive surface case, which also led both to dissipation of the cold pool from the edge inward and to a locally more vigorous and energetic CBL near the remnant cold pool's edge. Finally, the suppressed SHFs in the center that resulted from the land surface response slowed the CBL recovery there.

Since surface fluxes within the cold pools can either be suppressed or enhanced relative to the environment, the spatiotemporal surface flux patterns are more complex for land than for ocean surfaces studied previously (see references in section 1). DvdH17 even documented negative SHFs in the cold pool center where the ground was soaked by rain, an effect not incorporated in this study due to the exclusion of microphysical processes. Including rain influences on soil moisture and temperature would amplify our SHF suppression and further delay the CBL recovery at the cold pool center.

While we have documented generally suppressed LHF within the cold pool, LHF perturbations are likely to be highly sensitive to both the environment and surface conditions. For instance, both the r_v and LHF perturbations in the cold pool could reverse sign depending on whether the CBL is in a moistening or drying regime, which in turn depends on the ratio of the entrainment flux at the CBL top to the surface moisture flux (e.g., Mahrt, 1991; Mellado et al., 2017). Additionally, a rain-soaked ground can complicate the spatiotemporal LHF pattern within the cold pool (DvdH17). LHF patterns and the spatiotemporal structure of moisture within continental cold pools clearly merit further study.

Although we have simulated transient cold pools and excluded microphysical processes, the physics of the land surface-cold pool interactions, SHF spatial and temporal patterns, and dissipation of the cold pool from the edge inward should be robust for other scenarios, including for cold pools associated with active convection such as squall lines. In the squall line cases, the rate of cold pool dissipation or intensification would depend on the relative importance of the dissipation processes (surface heating and turbulent mixing) and replenishment processes (evaporative cooling). These scenarios were investigated by Trier et al. (1996) and Peters and Hohenegger (2017) for saturated or ocean surfaces but remain to be studied in semiarid continental environments, especially in the context of modulating factors such as wind shear, anvil shading, and precipitation effects on soil moisture. Additionally, the magnitude of the land surface-cold pool feedbacks demonstrated here is likely to be sensitive to uncertainties in the parameterization of surface-atmosphere energy exchanges.

Our results explicitly highlight the importance of utilizing a fully interactive land surface in process studies of cold pools, in agreement with recommendations by GvdH16, Gentine et al. (2016), and DvdH17. We speculate from these results that the reduced cold pool extent, faster dissipation, and altered CBL TKE recovery in the interactive surface case could, to first order, decrease the spatiotemporal scales of convective initiation, the spatial scales of boundary layer heterogeneity, and the probability of cold pool collisions. These speculations are supported by the findings reported in Trier et al. (1996) and Gentine et al. (2016) that including cold pool-surface interactions alters convective initiation and organization. Such important effects of interactive surfaces should be considered in forecasting applications and in cold pool parameterizations (e.g., Del Genio et al., 2015). Finally, nearly all cold pool-land surface interaction studies to date have exclusively utilized numerical models. New measurement techniques, such as the use of thermal imagery to measure spatiotemporal variability in surface fluxes (e.g., Lee et al., 2017; Morrison et al., 2017), are promising avenues with which to both validate modeling results and to extend process studies of cold pool-surface interactions to other environments.

Acknowledgments

L. D. Grant was funded by the National Science Foundation Graduate Research Fellowship Program (grant DGE-1321845) and NASA (grant NNN12AA01C). S. C. van den Heever was supported by the Office of Naval Research (grant N000141613093). The RAMS simulation output has been archived indefinitely in the Colorado State University Digital Repository and can be accessed at <https://hdl.handle.net/10217/186403>. We thank the two anonymous reviewers whose insightful comments and suggestions led to an improved manuscript.

References

- Achtmeier, G. L. (1991). Observations of turbulent boundary-layer interaction with a thunderstorm outflow—A possible wake region energy source. *Boundary-Layer Meteorology*, 55(4), 309–324. <https://doi.org/10.1007/BF00119807>
- Benjamin, T. B. (1968). Gravity currents and related phenomena. *Journal of Fluid Mechanics*, 31(2), 209–248. <https://doi.org/10.1017/S0022112068000133>
- Bryan, G. H., Wyngaard, J. C., & Fritsch, J. M. (2003). Resolution requirements for the simulation of deep moist convection. *Monthly Weather Review*, 131(10), 2394–2416. [https://doi.org/10.1175/1520-0493\(2003\)131%3C2394:RRFTSO%3E2.0.CO;2](https://doi.org/10.1175/1520-0493(2003)131%3C2394:RRFTSO%3E2.0.CO;2)

- Charba, J. (1974). Application of gravity current model to analysis of squall-line gust front. *Monthly Weather Review*, *102*(2), 140–156. [https://doi.org/10.1175/1520-0493\(1974\)102%3C0140:AOGCMT%3E2.0.CO;2](https://doi.org/10.1175/1520-0493(1974)102%3C0140:AOGCMT%3E2.0.CO;2)
- Chuda, T., Niino, H., Yoneyama, K., Katsumata, M., Ushiyama, T., & Tsukamoto, O. (2008). A statistical analysis of surface turbulent heat flux enhancements due to precipitating clouds observed in the tropical western Pacific. *Journal of the Meteorological Society of Japan*, *86*(3), 439–457. <https://doi.org/10.2151/jmsj.86.439>
- Computational and Information Systems Library (2012). *Yellowstone: IBM iDataPlex System (University Community Computing)*. Boulder, CO: National Center for Atmospheric Research. Retrieved from <http://n2t.net/ark:85065/d7wd3xhc>
- Cotton, W. R., Pielke, R. A., Walko, R. L., Liston, G. E., Tremback, C. J., Jiang, H., et al. (2003). RAMS 2001: Current status and future directions. *Meteorology and Atmospheric Physics*, *82*(1–4), 5–29. <https://doi.org/10.1007/s00703-001-0584-9>
- Couvreur, F., Rio, C., Guichard, F., Lothon, M., Canut, G., Bouniol, D., & Gounou, A. (2012). Initiation of daytime local convection in a semi-arid region analysed with high-resolution simulations and AMMA observations. *Quarterly Journal of the Royal Meteorological Society*, *138*(662), 56–71. <https://doi.org/10.1002/qj.903>
- de Szoeke, S. P., Skyllingstad, E. D., Zuidema, P., & Chandra, A. S. (2017). Cold pools and their influence on the tropical marine boundary layer. *Journal of the Atmospheric Sciences*, *74*(4), 1149–1168. <https://doi.org/10.1175/JAS-D-16-0264.1>
- Del Genio, A. D., Wu, J., & Chen, Y. (2012). Characteristics of mesoscale organization in WRF simulations of convection during TWP-ICE. *Journal of Climate*, *25*(17), 5666–5688. <https://doi.org/10.1175/JCLI-D-11-00422.1>
- Del Genio, A. D., Wu, J., Wolf, A. B., Chen, Y., Yao, M.-S., & Kim, D. (2015). Constraints on cumulus parameterization from simulations of observed MJO events. *Journal of Climate*, *28*(16), 6419–6442. <https://doi.org/10.1175/JCLI-D-14-00832.1>
- Drager, A. J., & van den Heever, S. C. (2017). Characterizing convective cold pools. *Journal of Advances in Modeling Earth Systems*, *9*, 1091–1115. <https://doi.org/10.1002/2016MS000788>
- Emanuel, K. A. (1994). *Atmospheric convection*. New York: Oxford University Press.
- Gentile, P., Garelli, A., Park, S., Nie, J., Torri, G., & Kuang, Z. (2016). Role of surface heat fluxes underneath cold pools. *Geophysical Research Letters*, *43*, 874–883. <https://doi.org/10.1002/2015GL067262>
- Grant, L. D., & van den Heever, S. C. (2016). Cold pool dissipation. *Journal of Geophysical Research: Atmospheres*, *121*, 1138–1155. <https://doi.org/10.1002/2015JD023813>
- Harrington, J. Y. (1997). The effects of radiative and microphysical processes on simulated warm and transition season Arctic stratus, (Doctoral dissertation). Fort Collins, CO: Colorado State University.
- Hill, G. E. (1974). Factors controlling the size and spacing of cumulus clouds as revealed by numerical and laboratory experiments. *Journal of the Atmospheric Sciences*, *31*(3), 646–673. [https://doi.org/10.1175/1520-0469\(1974\)031%3C0646:FCTSAS%3E2.0.CO;2](https://doi.org/10.1175/1520-0469(1974)031%3C0646:FCTSAS%3E2.0.CO;2)
- Johnson, R. H., & Nicholls, M. E. (1983). A composite analysis of the boundary layer accompanying a tropical squall line. *Monthly Weather Review*, *111*(2), 308–319. [https://doi.org/10.1175/1520-0493\(1983\)111%3C0308:ACAOTB%3E2.0.CO;2](https://doi.org/10.1175/1520-0493(1983)111%3C0308:ACAOTB%3E2.0.CO;2)
- Khairoutdinov, M., & Randall, D. (2006). High-resolution simulation of shallow-to-deep convection transition over land. *Journal of the Atmospheric Sciences*, *63*(12), 3421–3436. <https://doi.org/10.1175/JAS3810.1>
- Klemp, J. B., & Wilhelmson, R. B. (1978). The simulation of three-dimensional convective storm dynamics. *Journal of the Atmospheric Sciences*, *35*(6), 1070–1096. [https://doi.org/10.1175/1520-0469\(1978\)035%3C1070:TSOTDC%3E2.0.CO;2](https://doi.org/10.1175/1520-0469(1978)035%3C1070:TSOTDC%3E2.0.CO;2)
- Langhans, W., & Roms, D. M. (2015). The origin of water vapor rings in tropical oceanic cold pools. *Geophysical Research Letters*, *42*, 7825–7834. <https://doi.org/10.1002/2015GL065623>
- Lee, T. R., Buban, M., Dumas, E., & Baker, C. B. (2017). A new technique to estimate sensible heat fluxes around micrometeorological towers using small unmanned aircraft systems. *Journal of Atmospheric and Oceanic Technology*, *34*(9), 2103–2112. <https://doi.org/10.1175/JTECH-D-17-0065.1>
- Lilly, D. K. (1962). On the numerical simulation of buoyant convection. *Tellus*, *14*(2), 148–172. <https://doi.org/10.1111/j.2153-3490.1962.tb00128.x>
- Linden, P. F., & Simpson, J. E. (1986). Gravity-driven flows in a turbulent fluid. *Journal of Fluid Mechanics*, *172*(1), 481–497. <https://doi.org/10.1017/S0022112086001829>
- Louis, J.-F. (1979). A parametric model of vertical eddy fluxes in the atmosphere. *Boundary-Layer Meteorology*, *17*(2), 187–202. <https://doi.org/10.1007/BF00117978>
- Louis, J. F., Tiedtke, M., & Geleyn, J. F. (1981). A short history of the operational PBL-parameterization at ECMWF. In *Workshop on planetary boundary layer parametrization* (pp. 59–79). Shinfield Park, Reading, United Kingdom: ECMWF.
- Mahrt, L. (1991). Boundary-layer moisture regimes. *Quarterly Journal of the Royal Meteorological Society*, *117*(497), 151–176. <https://doi.org/10.1002/qj.49711749708>
- Mellado, J. P., Puche, M., & van Heerwaarden, C. C. (2017). Moisture statistics in free convective boundary layers growing into linearly stratified atmospheres. *Quarterly Journal of the Royal Meteorological Society*, *143*(707), 2403–2419. <https://doi.org/10.1002/qj.3095>
- Morrison, T. J., Calaf, M., Fernando, H. J. S., Price, T. A., & Pardyjak, E. R. (2017). A methodology for computing spatially and temporally varying surface sensible heat flux from thermal imagery. *Quarterly Journal of the Royal Meteorological Society*, *143*(707), 2616–2624. <https://doi.org/10.1002/qj.3112>
- Peters, K., & Hohenegger, C. (2017). On the dependence of squall-line characteristics on surface conditions. *Journal of the Atmospheric Sciences*, *74*(7), 2211–2228. <https://doi.org/10.1175/JAS-D-16-0290.1>
- Purdom, J. F. W. (1982). Subjective interpretation of geostationary satellite data for nowcasting. In K. Browning (Ed.), *Nowcasting* (pp. 149–166). London: Academic Press.
- Rieck, M., Hohenegger, C., & van Heerwaarden, C. C. (2014). The influence of land surface heterogeneities on cloud size development. *Monthly Weather Review*, *142*(10), 3830–3846. <https://doi.org/10.1175/MWR-D-13-00354.1>
- Robinson, F. J., Patterson, M. D., & Sherwood, S. C. (2013). A numerical modeling study of the propagation of idealized sea-breeze density currents. *Journal of the Atmospheric Sciences*, *70*(2), 653–668. <https://doi.org/10.1175/JAS-D-12-0113.1>
- Rotunno, R., Klemp, J. B., & Weisman, M. L. (1988). A theory for strong, long-lived squall lines. *Journal of the Atmospheric Sciences*, *45*(3), 463–485. [https://doi.org/10.1175/1520-0469\(1988\)045%3C0463:ATFSL%3E2.0.CO;2](https://doi.org/10.1175/1520-0469(1988)045%3C0463:ATFSL%3E2.0.CO;2)
- Saleeby, S. M., & van den Heever, S. C. (2013). Developments in the CSU-RAMS aerosol model: Emissions, nucleation, regeneration, deposition, and radiation. *Journal of Applied Meteorology and Climatology*, *52*(12), 2601–2622. <https://doi.org/10.1175/JAMC-D-12-0312.1>
- Saxen, T. R., & Rutledge, S. A. (1998). Surface fluxes and boundary layer recovery in TOGA COARE: Sensitivity to convective organization. *Journal of the Atmospheric Sciences*, *55*(17), 2763–2781. [https://doi.org/10.1175/1520-0469\(1998\)055%3C2763:SFABLR%3E2.0.CO;2](https://doi.org/10.1175/1520-0469(1998)055%3C2763:SFABLR%3E2.0.CO;2)
- Schlemmer, L., & Hohenegger, C. (2016). Modifications of the atmospheric moisture field as a result of cold-pool dynamics. *Quarterly Journal of the Royal Meteorological Society*, *142*(694), 30–42. <https://doi.org/10.1002/qj.2625>

- Smagorinsky, J. (1963). General circulation experiments with the primitive equations. I. The basic experiment. *Monthly Weather Review*, *91*(3), 99–164. [https://doi.org/10.1175/1520-0493\(1963\)091%3C0099:GCEWTP%3E2.3.CO;2](https://doi.org/10.1175/1520-0493(1963)091%3C0099:GCEWTP%3E2.3.CO;2)
- Tompkins, A. M. (2001). Organization of tropical convection in low vertical wind shears: The role of cold pools. *Journal of the Atmospheric Sciences*, *58*(13), 1650–1672. [https://doi.org/10.1175/1520-0469\(2001\)058%3C1650:OOTCIL%3E2.0.CO;2](https://doi.org/10.1175/1520-0469(2001)058%3C1650:OOTCIL%3E2.0.CO;2)
- Trier, S. B., Skamarock, W. C., LeMone, M. A., Parsons, D. B., & Jorgensen, D. P. (1996). Structure and evolution of the 22 February 1993 TOGA COARE squall line: Numerical simulations. *Journal of the Atmospheric Sciences*, *53*(20), 2861–2886. [https://doi.org/10.1175/1520-0469\(1996\)053%3C2861:SAEOTF%3E2.0.CO;2](https://doi.org/10.1175/1520-0469(1996)053%3C2861:SAEOTF%3E2.0.CO;2)
- Walko, R. L., Band, L. E., Baron, J., Kittel, T. G. F., Lammers, R., Lee, T. J., et al. (2000). Coupled atmosphere–biophysics–hydrology models for environmental modeling. *Journal of Applied Meteorology*, *39*(6), 931–944. [https://doi.org/10.1175/1520-0450\(2000\)039%3C0931:CABHMF%3E2.0.CO;2](https://doi.org/10.1175/1520-0450(2000)039%3C0931:CABHMF%3E2.0.CO;2)
- Young, G. S., Perugini, S. M., & Fairall, C. W. (1995). Convective wakes in the equatorial western Pacific during TOGA. *Monthly Weather Review*, *123*(1), 110–123. [https://doi.org/10.1175/1520-0493\(1995\)123%3C0110:CWITEW%3E2.0.CO;2](https://doi.org/10.1175/1520-0493(1995)123%3C0110:CWITEW%3E2.0.CO;2)